The Astronomical Journal, 164:129 (15pp), 2022 October https://doi.org/10.3847/1538-3881/ac83af

Tracers of Dense Gas in the Outer Galaxy

Sudeshna Patra[1], Neal J. Evans II[2,3,4], Kee-Tae Kim[3,5], Mark Heyer[6], Jens Kauffmann[7], Jessy Jose[1],
Manash R. Samal[8], and Swagat R. Das[1]
[1] Indian Institute of Science Education and Research (IISER) Tirupati, Rami Reddy Nagar, Karakambadi Road, Mangalam (P.O.), Tirupati 517507, India
inspire.sudeshna@gmail.com
[2] Department of Astronomy, The University of Texas at Austin, 2515 Speedway, Stop C1400 Austin, Texas 78712-1205, USA
[3] Korea Astronomy and Space Science Institute, 776 Daedeokdae-ro, Yuseong-gu Daejeon, 34055, Republic of Korea
[4] Humanitas College, Global Campus, Kyung Hee University, Yongin-shi 17104, Republic of Korea
[5] University of Science and Technology, Korea (UST), 217 Gajeong-ro, Yuseong-gu, Daejeon 34113, Republic of Korea
[6] Department of Astronomy, University of Massachusetts Amherst, Amherst, MA 01003, USA
[7] Haystack Observatory, MIT, 99 Milstone Road, Westford, MA 01886 USA
[8] Astronomy & Astrophysics Division, Physical Research Laboratory, Ahmedabad, 380009, State of Gujarat, India

Received 2022 April 4; revised 2022 July 6; accepted 2022 July 21; published 2022 September 7

Abstract

We have mapped HCN and HCO$^+$ ($J = 1 \rightarrow 0$) line emission toward a sample of seven star-forming regions (with $12 + \log[\mathrm{O/H}]$ ranging from 8.34 to 8.69) in the outer Milky Way (Galactocentric distance >9.5 kpc), using the 14 m radio telescope of the Taeduk Radio Astronomy Observatory. We compare these two molecular lines with other conventional tracers of dense gas, millimeter-wave continuum emission from dust and extinction thresholds ($A_V \geqslant 8$ mag), inferred from the ^{13}CO line data. HCN and HCO$^+$ correlate better with the millimeter emission than with the extinction criterion. A significant amount of luminosity comes from regions below the extinction criterion and outside the millimeter clump for all the clouds. The average fraction of HCN luminosity from within the regions with $A_V \geqslant 8$ mag is 0.343 ± 0.225; for the regions of millimeter emission, it is 0.478 ± 0.149. Based on a comparison with column density maps from Herschel, HCN and HCO$^+$ trace dense gas in high column density regions better than does ^{13}CO. HCO$^+$ is less concentrated than HCN for outer Galaxy targets, in contrast with the inner Galaxy sample, suggesting that metallicity may affect the interpretation of tracers of dense gas. The conversion factor between the dense gas mass (M_{dense}) and line luminosities of HCN and HCO$^+$, when integrated over the whole cloud, is comparable to factors used in extragalactic studies.

Unified Astronomy Thesaurus concepts: Star forming regions (1565); Molecular clouds (1072)

1. Introduction

Detailed observation of molecular clouds in the Milky Way (Heiderman et al. 2010; Lada et al. 2010, 2012; Evans et al. 2014; Vutisalchavakul et al. 2016) and studies of external galaxies (Gao & Solomon 2004a) have shown that star formation is more accurately predicted by the amount of dense molecular gas rather than by the total amount of molecular gas. The molecules with high dipole moment and high critical density, such as HCN and HCO$^+$, are used as dense gas tracers. The pioneering studies by Gao & Solomon (2004a, 2004b) revealed a tight linear correlation between the luminosity of the HCN $J = 1 \rightarrow 0$ transition (as a tracer of the mass of dense molecular gas) and the far-infrared luminosity, indicative of the star formation rate (SFR) for whole galaxies. Later works extended this relation to resolved structures in other galaxies (Jiménez-Donaire et al. 2019; Heyer et al. 2022) or even to massive clumps in the Milky Way (Wu et al. 2005; Liu et al. 2016; Stephens et al. 2016; Shimajiri et al. 2017).

Recent studies (Kauffmann et al. 2017; Pety et al. 2017; Evans et al. 2020; Nguyen-Luong et al. 2020) have questioned how well the lowest-J transitions of HCN and HCO$^+$ trace the dense gas. These authors report that HCN and HCO$^+$ $J = 1 \rightarrow 0$ emission is easily detectable from the diffuse part of the cloud with typical density 100–500 cm^{-3}. The concept of detecting a particular line above or around the critical density (n_c) is oversimplified (Evans 1989). In reality, multilevel excitation effects and radiative trapping effects all tend to lower the effective excitation density (n_{eff}), defined as the density needed to detect a molecular line with integrated intensity of 1 K km s^{-1} (Evans 1999; Shirley 2015). For the low-J transitions the effective excitation densities are typically 1–2 orders of magnitude lower than the critical densities. The values of n_{eff} for HCN and HCO$^+$ are 4.5×10^3 cm^{-3} and 5.3×10^2 cm^{-3} at 20 K, respectively (Shirley 2015). For modern surveys with low rms noise, lines at the detection limits can be produced by gas with density as low as 50–100 cm^{-3}, explaining the emission from extended translucent regions where the density of gas is much lower than the critical densities of HCN and HCO$^+$ (Evans et al. 2020).

Pety et al. (2017) found that only a small fraction of the luminosity of HCN (18%) and HCO$^+$ (16%) arises from regions with $A_V > 15$ mag for Orion B. Kauffmann et al. (2017) found that HCN ($J = 1 \rightarrow 0$) mainly traces gas with $A_V \approx 6$ mag, or $n \approx 870$ cm^{-3} toward Orion A. A substantial fraction (44%–100%) of the total line luminosities of HCN and HCO$^+$ arise outside the $A_V > 8$ mag region often associated with star formation for six inner Galaxy clouds (Evans et al. 2020). Most dense cores and young stellar objects (YSOs) are found at $A_V \geqslant 8$ mag (Heiderman et al. 2010; Lada et al. 2010, 2012).

None of the studies described above considered the star-forming regions in the outer Galaxy, i.e., clusters having Galactocentric distance (R_G) greater than ∼8.2 kpc. The star-forming regions in the outer Galaxy (low-density regime) behave distinctively from the environment around the solar neighborhood (intermediate-density regime) and also from the

Table 1
Sample of Clouds

Target	l (deg)	b (deg)	R_G (kpc)	D (kpc)	m_{cloud} ($10^4\ M_\odot$)	SpT (Ref)	12 + log(O/H) (Ref)	Map Size (arcmin × arcmin)	A_V[d] (mag)
S206[a]	150.5886	−0.8570	$10.88^{+0.25}_{-0.26}$	$2.96^{+0.17}_{-0.15}$	18.5	O4V (1)	8.37 (8)	15 × 15	1.0
S208[a]	151.3098	1.9045	$11.87^{+0.37}_{-0.34}$	$4.02^{+0.27}_{-0.25}$	6.8	B0V (2)	8.43 (8)	10 × 20	0.3
S212[b]	155.3375	2.6345	14.76 ± 1.30	$6.65^{+1.36}_{-1.26}$	19.0	O7 (3)	8.34 (9)	13 × 14	0.5
S228[c]	169.1432	−1.0475	10.72 ± 0.19	2.56 ± 0.09	11.6	O8V (4)	8.39 (8)	11 × 33	0.4
S235[b]	173.6682	2.7799	$9.85^{+0.16}_{-0.17}$	1.66 ± 0.07	41.1	O9.5V (5)	8.54 (8)	30 × 30	1.5
S252[c]	189.8418	0.3156	$10.09^{+0.12}_{-0.11}$	$1.92^{+0.12}_{-0.11}$	49.0	O6.5V,O9.5V,B V (6)	8.51 (8)	30 × 30	1.5
S254[c]	192.7935	0.0290	10.13 ± 0.21	$1.96^{+0.12}_{-0.09}$	51.5	O9.5V,B0.5V (7)	8.69 (8)	50 × 34	1.5

References. (1) Maíz Apellániz et al. 2016; (2) Moffat et al. 1979; (3) Sota et al. 2014; (4) Chini & Wink 1984; (5) Georgelin et al. 1973; (6) Jose et al. 2012; (7) Ojha et al. 2011; (8) Wang et al. 2018; (9) Méndez-Delgado et al. 2022.

Data availability:

[a] ^{12}CO, ^{13}CO.

[b] ^{12}CO, ^{13}CO, BGPS.

[c] ^{12}CO, ^{13}CO, BGPS, Herschel.

[d] A_V values corresponding to the threshold value of 5 times the rms noise in the ^{13}CO map.

Central Molecular Zone (CMZ, high-density regime; Kennicutt & Evans 2012). The physical and chemical conditions in star-forming regions are dependent on the environment, which is in turn a function of Galactocentric radius (R_G).

The Milky Way and other normal spiral galaxies are known to have a negative gradient of metallicity with R_G (Searle 1971). Many studies have found a radial abundance gradient of oxygen, nitrogen, etc., in the Milky Way (Deharveng et al. 2000; Esteban et al. 2017; Esteban & Garcia-Rojas 2018). Most recently, Méndez-Delgado et al. (2022) report linear radial abundance gradients for O/H and N/H with slopes of -0.044 ± 0.009 dex kpc^{-1} and -0.063 ± 0.009 dex kpc^{-1}, respectively, for $R_G = 4.88$–17 kpc, and for C/H the slope is -0.077 ± 0.019 dex kpc^{-1} for $R_G = 6.46$–11.6 kpc. The efficiency of gas cooling and dust shielding processes decreases at lower metallicity, thereby affecting the condensation and fragmentation of giant molecular clouds (GMCs). Conversely, the lower interstellar radiation field and cosmic-ray fluxes at larger R_G decrease the gas heating (Balser et al. 2011). The balance between these processes sets the gas and dust physical conditions and may cause different star formation outcomes from those in the CMZ or solar neighborhood. While studies of nearby galaxies (LMC, SMC) with low metallicity are used to understand these effects (Galametz et al. 2020), the outer Milky Way is much closer to us. The outer Galaxy targets provide a less confusing view of the interstellar medium (ISM), as they are widely separated and there is no blending of emission. This clear perspective of the outer Galaxy enables studies of individual GMCs from which global properties of star formation can be estimated. Thus, studying the star-forming regions in the outer Galaxy can bridge the gap between the star formation studies in Galactic and extragalactic environments.

To inform interpretation of extragalactic studies, we investigate the distribution of HCN and HCO$^+$ $J = 1 \rightarrow 0$ emission over the full area of molecular clouds and range of physical conditions. This work, focusing on the outer Galaxy, complements the inner Galaxy work (Evans et al. 2020).

2. Sample

We selected seven targets beyond the solar circle with $R_G > 9.5$ kpc with diversity in properties such as cloud mass, physical size, number of massive stars, metallicity, etc. (see Table 1). We also considered the availability of molecular data (^{12}CO and ^{13}CO emission from the Extended Outer Galaxy survey; Section 3.2), dust emission from the Bolocam Galactic Plane Survey (BGPS; Ginsburg et al. 2013), and FIR emission from Herschel data (Marsh et al. 2017). Several distance values are available in the literature based on kinematic or stellar measurements. In order to maintain uniformity, we adopt the GAIA EDR3–based distance values of all the targets (except S252) from Méndez-Delgado et al. (2022) and use the same methodology to obtain the distance for S252. The distance of the Sun from the Galactic center is taken as 8.2 kpc (Gravity Collaboration et al. 2019). R_G values of our sample range between 9.85 and 14.76 kpc (see Table 1).

The spectral type(s) (SpT) of the main ionizing star(s) and 12 + log[O/H] values of each target and their respective references are also given in Table 1. We mapped the HCN and HCO$^+$ ($J = 1 \rightarrow 0$) emission from the parent clouds of seven H II regions over an area based on ^{13}CO emission (see details in Section 3). The cloud mass (M_{cloud}) is obtained using the CO data described in Section 3 and $M_{\text{cloud}} = \alpha_{\text{CO}} L_{\text{CO}}$ with $\alpha_{\text{CO}} = 4.3\ M_\odot\ (\text{Kkms}^{-1}\text{pc}^2)^{-1}$, where L_{CO} is the luminosity expressed in K km s^{-1} pc^2 (Bolatto et al. 2013). A brief description of each region can be found in Appendix A.

3. Observations and Data Sets

3.1. HCN and HCO$^+$ Observations with TRAO

We mapped the seven outer Galaxy clouds in the HCN ($J = 1 \rightarrow 0$, 88.631847 GHz) and HCO$^+$ ($J = 1 \rightarrow 0$, 89.1885296 GHz) lines simultaneously at Taeduk Radio Astronomy Observatory (TRAO) in 2020 January. The TRAO telescope is equipped with the SEcond QUabbin Optical Image Array (SEQUOIA-TRAO), a multibeam receiver with 16 pixels in a 4 × 4 array, and operates in the 85−115 GHz range. The back end has a 2G fast Fourier transform (FFT) spectrometer. The instrumental properties are described in Jeong et al. (2019). The TRAO has a main-beam size of 58″ at these frequencies and a main-beam efficiency (defined so that $T_{\text{mb}} = T_A^*/(f_b \eta_{\text{mb}})$, where T_{mb} is the Rayleigh–Jeans main-beam temperature and f_b is the fraction of the beam filled by the source) of 46% at 89 GHz (Jeong et al. 2019). The individual SEQUOIA beams vary in beam size (efficiency) by only a few arcseconds (few percent). The beams are very circular, and beam efficiencies vary less than 3% with elevation angle.

We used the on-the-fly (OTF) mode to map the clouds. The mapped areas for the individual targets were determined from maps of their ^{13}CO ($J = 1 \rightarrow 0$) line emission. We used a threshold value of 5 times the rms noise in the ^{13}CO map to estimate the mapping area for HCN and HCO$^+$ from the TRAO 14 m telescope. The A_V values corresponding to the threshold values are listed in Table 1. All the targets were mapped in Galactic coordinates. The mapped areas for individual targets are listed in Table 1.

The system temperature was ∼190 K during HCN and HCO$^+$ observations. We used SiO maser sources at 86 GHz for pointing and focusing the telescope every 3 hr. We smoothed the data with the boxcar function to a velocity resolution of about 0.2 km s^{-1}, resulting in an rms sensitivity of 0.06–0.08 K on the T_A^* scale for all the targets. We obtained ∼150 hr of observations in total.

The following steps were done to reduce the data. We used the OTFTOOL to read the raw OTF data for each map of each tile and then converted them into the CLASS format map after subtracting a first-order baseline. We applied noise weighting and chose the output cell size of 20″ in OTFTOOL. We did not apply any convolution function to make the maps, so the effective beam size is the same as the main-beam size. Further reduction was done in the CLASS format of GILDAS,[9] where we chose the velocity range (v_{sp}) to get good baselines on each side of the velocity range of significant emission (v_{win}). The reduction details are listed in Appendix B, Table B1. We subtracted a second-order polynomial baseline and converted those files to FITS format using GREG.

3.2. Ancillary Data Available

For this work, we have also used the following data sets :

1. ^{12}CO and ^{13}CO ($J = 1 \rightarrow 0$) Observations: ^{12}CO and ^{13}CO data for all the targets are extracted from the Exeter-FCRAO Extended Outer Galaxy survey using the Five College Radio Astronomy Observatory (FCRAO) 14 m telescope. The EXFC survey covered ^{12}CO and ^{13}CO $J = 1 \rightarrow 0$ emission within two longitude ranges: $55° < l < 100°$ with Galactic latitude range $-1.°4 \leqslant b \leqslant +1.°9$ and $135° < l < 195°$ with Galactic latitude range $-3.°6 < b < 5.°6$ (Roman-Duval et al. 2016). Our outer Galaxy targets are covered by the latter survey. The angular resolutions of ^{12}CO and ^{13}CO are 45″ and 48″, respectively, and the grid size is 22.″5. The spectral resolution is 0.127 km s^{-1}. All of the data have been deconvolved to remove contributions from the antenna error beam and therefore are in main-beam temperature units.
2. Millimeter Dust Continuum Emission: We use 1.1 mm continuum emission data from the BGPS[10] using Bolocam on the Caltech Submillimeter Observatory. The BGPS does not cover the outer Galaxy regions uniformly; it covers four targeted regions (IC 1396, a region toward the Perseus arm, W3/4/5, and Gem OB1). The effective resolution of this survey is 33″. We use the mask files of the sources from the V2.1 table,[11] where the pixel values in the mask file are set with the catalog number where the source is above the 2σ threshold; otherwise, the pixel values are zero (Ginsburg et al. 2013). The Bolocat V2.1 contains the 1.1 mm photometric flux of 8594 sources for the aperture radii of 20″, 40″, and 60″ and it also provides flux densities integrated over the source area. As this is not a contiguous survey toward the outer Galaxy, not all the targets have BGPS data. The data availability of the targets is indicated by the footnotes in Table 1.
3. Far-Infrared Data: We have used the column density maps determined from Herschel data (Marsh et al. 2017) and available at the Herschel infrared Galactic Plane (Hi-GAL) survey site table.[12] These column density maps are derived using the PPMAP procedure (Marsh et al. 2015) on the continuum data in the wavelength range 70–500 μm from the Hi-GAL survey. The spatial resolution of the maps is 12″. Not all the targets in our list are covered by the Hi-GAL survey. Table 1 shows the data availability.

4. Results and Analysis

Our goal is to compare the luminosities of HCN and HCO$^+$ $J = 1 \rightarrow 0$ transitions to other conventional tracers of dense gas, in particular extinction thresholds and millimeter-wave emission from dust. We estimate the extinction from the ^{13}CO data and relations between gas column density and extinction. For the emission from dust, we use the mask file of the BGPS data, an indicator of the existence of gas of relatively high volume density (Dunham et al. 2011). We also examine the ability of HCN, HCO$^+$, and ^{13}CO to trace column density, determined from Herschel maps.

4.1. Luminosity Calculation Based on Extinction Criterion

This section describes the method of calculating luminosity of the line tracers coming from the dense regions and also from outside the dense region, depending on a ^{13}CO column density based extinction (A_V) map. It consists of two main steps: (i) making molecular hydrogen column density (N(H$_2$)) maps of each target, convertible into maps of A_V; and (ii) measuring the luminosity of regions satisfying the A_V criterion.

4.1.1. Identifying the Pixels with $\mathrm{A_V} \geqslant 8$ mag

To derive the molecular hydrogen column density maps of each target, we use their ^{12}CO and ^{13}CO data. We first identify the velocity range by examining the spectrum of ^{13}CO emission averaged over the whole mapped region of each target. The method of making column density maps of ^{13}CO is discussed in detail in Appendix C. We follow Equations (C1)–(C5) from Appendix C to produce the total column density map of ^{13}CO (N(^{13}CO)) using ^{13}CO and ^{12}CO data. Next, we convolve and regrid the ^{13}CO column density map to match the TRAO map and convert it to a molecular hydrogen column density map using the following equation:

$$N(\mathrm{H_2}) = N(^{13}\mathrm{CO})\left[\frac{\mathrm{H_2}}{\mathrm{CO}}\right]\left[\frac{\mathrm{CO}}{^{13}\mathrm{CO}}\right]. \quad (1)$$

We assume a fractional abundance of 6000 for CO (Lacy et al. 2017), and we apply the [^{12}C]/[^{13}C] isotopic ratio recently

---

[9] https://www.iram.fr/IRAMFR/GILDAS/

[10] https://doiorg/1026131/irsa482

[11] https://irsa.ipac.caltech.edu/data/BOLOCAM_GPS/

[12] http://www.astro.cardiff.ac.uk/research/ViaLactea/

derived by Jacob et al. (2020). This ratio is linearly dependent on the Galactocentric distance (R_G) of the target:

$$\frac{[^{12}\mathrm{C}]}{[^{13}\mathrm{C}]} = 5.87 \times \frac{R_G}{\mathrm{kpc}} + 13.25. \quad (2)$$

Finally, we use the relation $A_V = 1.0 \times 10^{-21} N(\mathrm{H}_2)$ to convert the molecular hydrogen column density to extinction (Lacy et al. 2017). This procedure allows us to define the pixels satisfying the criterion: $A_V \geqslant 8$ mag.

4.1.2. The Emission from the Total Region and Inside Region with $\mathrm{A_V} \geqslant 8$ mag

Next, we calculate the average spectrum for two regions: (1) including all pixels in the dense region, and (2) all pixels outside the dense region based on the A_V criterion ($1.5\ \mathrm{mag} \leqslant A_V < 8$ mag). The lower limit on A_V is based on 5 times the rms noise threshold in the ^{13}CO maps. Because the rms noise levels are not the same for all the clouds (see Table 1), we use $A_V = 1.5$ mag as the lower limit to make the analysis uniform.

We first identify the dense regions with $A_V \geqslant 8$ mag in the extinction map (denoted by "in"). Figure 1 shows the integrated intensity map of HCN and HCO$^+$ for all the targets; white contours on each image in Figure 1 indicate the $A_V \geqslant 8$ mag regions. The spectra averaged over pixels that satisfy the criterion $A_V \geqslant 8$ mag (blue line) and the spectra for pixels that do not (denoted "out" and shown in red line) are shown in Figure 2 (panels (a) and (b) and upper panels of panels (c), (d), (e), (f), and (g)). Figure 2 (S212) does not show any blue line in the upper panel because there is no pixel satisfying the $A_V \geqslant 8$ mag criterion. The average spectral lines from the "in" region are stronger than those from the "out" region whenever both spectra are available. One odd feature appears in Figure 1 (S228): the HCN and HCO$^+$ agree well with the BGPS, but there is no peak in A_V in that region. Figure 2 (S228) does not show strong emission for HCN and HCO$^+$ at the position of the $A_V \geqslant 8$ mag region (upper panel). This oddity and other information regarding individual targets are described in Appendix A.

For the calculation of luminosity, we use the main-beam-corrected temperature of species X ($T_X = T_A^*/\eta_{mb}$, where $\eta_{mb} = 0.46$). The velocity ranges for ^{13}CO and HCO$^+$ are similar, and for HCN we expand the velocity range to account for the hyperfine structure (around 3–6 km s^{-1} on each side depending on the target requirements). The velocity ranges are explained in Appendix B.

We measure the luminosity of species X arising from the $A_V \geqslant 8$ mag region using the following equation:

$$L_{\mathrm{X,in}} = D^2 \int_{v_{\mathrm{sp,l}}}^{v_{\mathrm{sp,u}}} dv \int d\Omega_{\mathrm{in}} T_X(l, b, v), \quad (3)$$

where D is the distance of the target from the Sun in pc and the integrals are taken over the line velocity between $v_{\mathrm{sp,l}}$ and $v_{\mathrm{sp,u}}$, the lower and upper limits of the line spectral window, and the solid angle that satisfies the extinction criterion. In practice, we use the average spectrum in Figure 2 to define the integrated intensity

$$I_{\mathrm{X}} = \int_{v_{\mathrm{sp,l}}}^{v_{\mathrm{sp,u}}} T_X dv \quad (4)$$

and compute the luminosity from the following equation:

$$L_{\mathrm{X,in}} = D^2 I_{\mathrm{X}} N_{\mathrm{in}} \Omega_{\mathrm{pix}}, \quad (5)$$

where N_{in} is the number of pixels satisfying the "in" condition and Ω_{pix} is the solid angle of a pixel.

The uncertainty in luminosity is

$$\sigma_L = D^2 \delta v \sqrt{N_{\mathrm{ch}}}\ \sigma_{T_X}\ N_{\mathrm{in}} \Omega_{\mathrm{pix}}, \quad (6)$$

where N_{ch} is the number of channels in the line region, δv is the channel width, and σ_{T_X} is the rms noise in the baseline of the average spectrum.

To calculate the total luminosity ($L_{\mathrm{X,tot}}$), we follow the same method but include all pixels with $A_V > 1.5$ mag for $L_{\mathrm{X,tot}}$.

We follow the same procedure for HCN, HCO$^+$, and ^{13}CO; for ^{13}CO, we made integrated intensity maps for the specified velocity range using the FITS files from FCRAO, and these maps are convolved, resampled, and aligned with the TRAO maps.

We tabulated the values for the fraction of pixels inside the A_V criterion ($N_{\mathrm{in}}/N_{\mathrm{tot}}$), the log of total line luminosity (Log L_{tot}), the log of the line luminosity coming from the $A_V \geqslant 8$ mag region (Log L_{in}), and the fractional luminosity ($f_L = L_{\mathrm{in}}/L_{\mathrm{tot}}$) in Table 2 for HCN, HCO$^+$ and ^{13}CO. Also we have given the statistical parameters (mean, standard deviation, and median) for the relevant columns. S212 has no pixels with $A_V \geqslant 8$ mag.

Figure 3(a) shows f_L within the "in" regions defined by $A_V \geqslant 8$ mag (left) for each cloud sorted by increasing metallicity. The values of f_L vary between 0.014 and 0.661 for HCN, between 0.009 and 0.608 for HCO$^+$, and between 0.018 and 0.570 for ^{13}CO. The values of f_L for HCN are higher than those for HCO$^+$ and ^{13}CO. The mean value of the line luminosities coming from the "in" region is higher by 0.12 for HCN compared to HCO$^+$. For ^{13}CO, L_{in} is higher but the values of fractional luminosity (f_L) are lower than those of HCN and HCO$^+$. In terms of the logarithm of the total line luminosity, the mean is 2.78 for ^{13}CO, 1.98 for HCO$^+$, and 1.99 for HCN. Comparing the two dense gas tracers, HCO$^+$ and HCN provide similar total luminosity, but HCN shows better correlation with the extinction criterion in terms of f_L followed by HCO$^+$ and ^{13}CO (see Figure 3(a)).

The correlation between fractional line luminosity (f_L) arising from the $A_V \geqslant 8$ mag region with Log L_{tot} and Log L_{in} (Figure 4) shows that the clouds with more material (i.e., higher luminosity) tend to have higher values of f_L.

4.2. Luminosity Calculation from BGPS

In this section, we follow the same basic method but use the dust thermal continuum emission to trace the "dense" gas. We use the data from BGPS to compare the line tracers in those regions. Millimeter continuum dust emission remains an optically thin tracer of the gas column density even in dense molecular clouds and efficiently identifies the molecular clumps that are possible sites of star formation. Because of

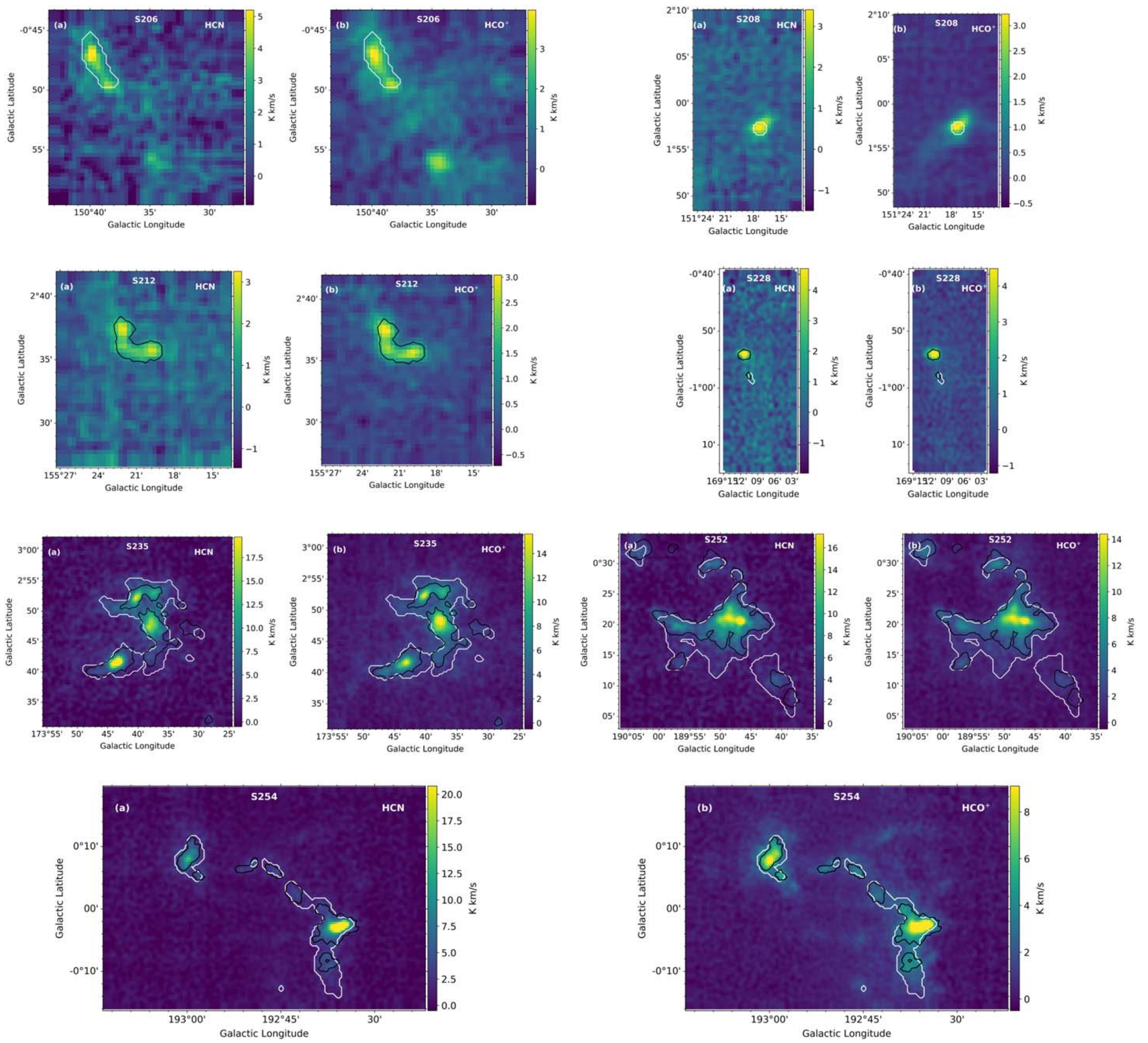

Figure 1. This figure shows the integrated intensity map of (a) HCN and (b) HCO$^+$ for each target (names of each target are mentioned in each image). The white contours indicate the $A_V \geqslant 8$ mag regions, and black contours indicate the BGPS mask regions. There are no black contours in S206 and S208, as they lack BGPS data. There is no white contour in S212, as there is no region above $A_V = 8$ mag.

the limits on sensitivity to large angular scale emission, the BGPS emission traces volume density, but the characteristic density probed decreases with distance (Dunham et al. 2011). For distances in this sample of 2–6 kpc, the mean density traced is 5×10^3 cm^{-3} to 1×10^4 cm^{-3} (Figure 12 of Dunham et al. 2011) with properties of clumps rather than cores or clouds. We use the mask maps of BGPS, downloaded from Bolocat V2.1, to define the “in” region. As before, we then computed the line luminosities inside and outside the mask regions.

First, we changed the BGPS mask maps to the same resolution and pixel size as the TRAO maps. Next, we make the average spectra of the "in" and "out" regions and use Equation (5) to calculate the luminosity for HCN, HCO$^+$, and ^{13}CO. The total luminosities ($L_{\rm tot}$) are the same as those obtained using the extinction condition $A_V \geqslant 8$ mag in Section 4.1.

Among all the targets, five of the regions are covered by the BGPS. The black contours on the integrated intensity maps of HCN and HCO$^+$ in Figure 1 show the position of the BGPS inner region. The bottom panels of Figure 2 (panels (c), (d), (e), (f), (g)) show the average spectra of the luminosities coming from the BGPS “in” and “out” regions. All five targets show clear detection of HCN and HCO$^+$ from the BGPS mask region, but significant emission is coming from outside the BGPS mask regions.

We present the result of those five targets in Table 3, along with the mean, standard deviation, and median for relevant columns. We have listed the values for the fraction of pixels

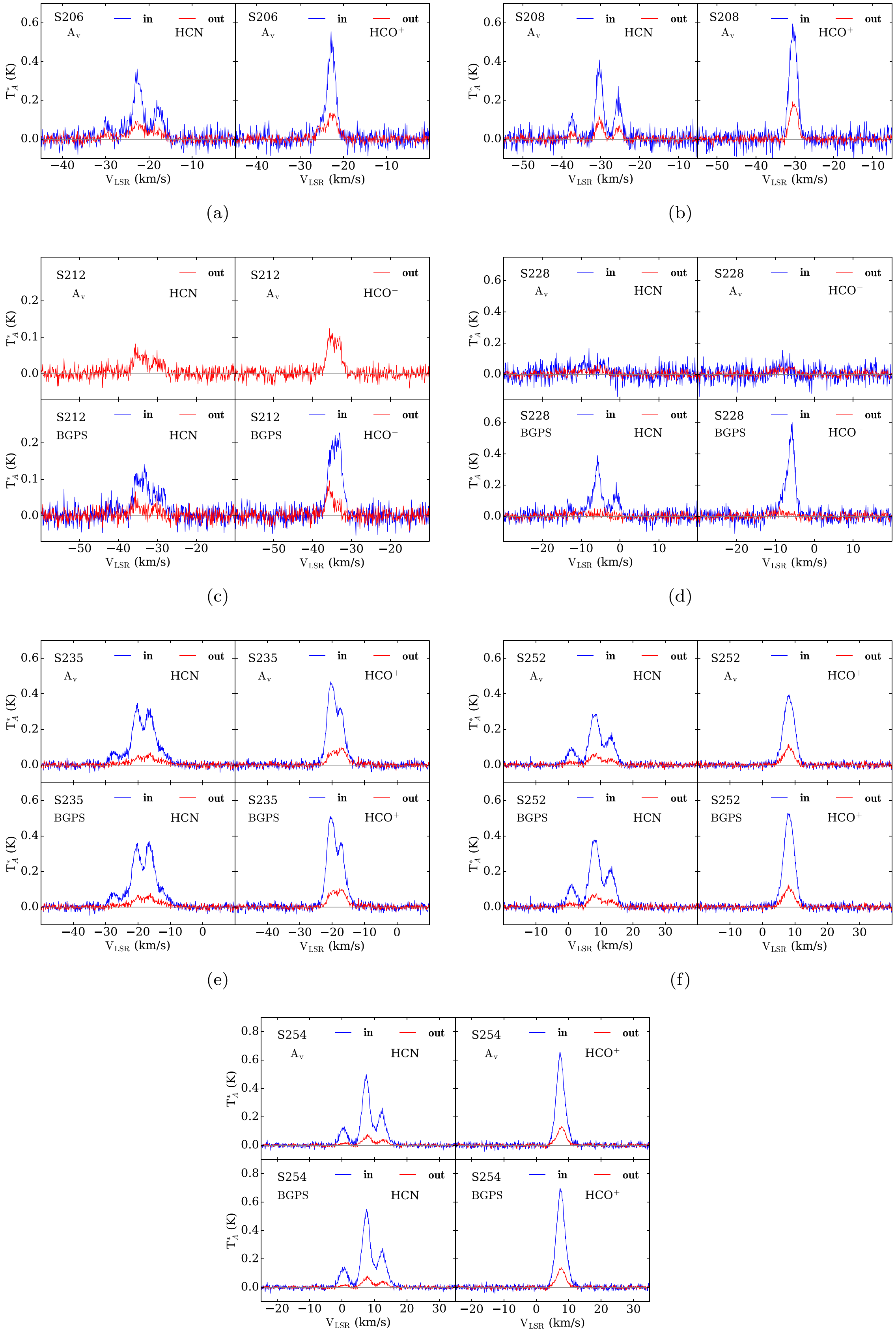

(a) (b) (c) (d) (e) (f) (g)

Figure 2. This is the average spectrum plot for the clouds (a) S206, (b) S208, (c) S212, (d) S228, (e) S235, (f) S252, and (g) S254 based on the A_V criterion and BGPS mask map. The left panel in all images is for HCN, and the right panel is for HCO$^+$. The blue line indicates the line emission coming from $A_V \geqslant 8$ mag regions, and the red line indicates the emission from 1.5 mag $\leqslant A_V < 8$ mag regions in the upper panel of each panel. In the lower panel of each panel (except panels (a) and (b)), the blue line indicates emission coming from the BGPS masked region, and the red line is for emission outside the masked region.

Table 2
Line Luminosities versus $A_V \geqslant 8$ mag

Source	$N_{\mathrm{in}}/N_{\mathrm{tot}}$	Log L_{tot} HCN	Log L_{in} HCN	f_L HCN	Log L_{tot} HCO$^+$	Log L_{in} HCO$^+$	f_L HCO$^+$	Log L_{tot} ^{13}CO	Log L_{in} ^{13}CO	f_L ^{13}CO
S206	0.067	$1.88^{+0.05}_{-0.05}$	$1.14^{+0.05}_{-0.05}$	0.180 (0.008)	$1.84^{+0.05}_{-0.05}$	$1.05^{+0.05}_{-0.05}$	0.164 (0.006)	$2.54^{+0.05}_{-0.05}$	$1.76^{+0.05}_{-0.05}$	0.167 (0.004)
S208	0.061	$1.31^{+0.06}_{-0.06}$	$0.63^{+0.06}_{-0.06}$	0.209 (0.011)	$1.39^{+0.05}_{-0.06}$	$0.62^{+0.05}_{-0.06}$	0.170 (0.004)	$2.04^{+0.05}_{-0.06}$	$1.18^{+0.07}_{-0.07}$	0.138 (0.014)
S212	…	$1.89^{+0.15}_{-0.21}$	…	…	$1.95^{+0.15}_{-0.21}$	…	…	$2.49^{+0.15}_{-0.21}$	…	…
S228	0.008	$1.40^{+0.05}_{-0.05}$	$-0.44^{+0.08}_{-0.09}$	0.014 (0.003)	$1.29^{+0.04}_{-0.05}$	$-0.75^{+0.10}_{-0.13}$	0.009 (0.002)	$2.77^{+0.03}_{-0.03}$	$1.02^{+0.07}_{-0.08}$	0.018 (0.003)
S235	0.164	$2.45^{+0.04}_{-0.04}$	$2.18^{+0.03}_{-0.04}$	0.537 (0.011)	$2.43^{+0.03}_{-0.04}$	$2.10^{+0.03}_{-0.04}$	0.471 (0.007)	$3.09^{+0.03}_{-0.04}$	$2.64^{+0.03}_{-0.04}$	0.355 (0.002)
S252	0.265	$2.53^{+0.05}_{-0.05}$	$2.35^{+0.05}_{-0.05}$	0.661 (0.025)	$2.48^{+0.05}_{-0.05}$	$2.27^{+0.05}_{-0.05}$	0.608 (0.010)	$3.32^{+0.05}_{-0.05}$	$3.08^{+0.05}_{-0.05}$	0.570 (0.003)
S254	0.107	$2.50^{+0.05}_{-0.04}$	$2.16^{+0.05}_{-0.04}$	0.459 (0.008)	$2.49^{+0.05}_{-0.04}$	$2.06^{+0.05}_{-0.04}$	0.371 (0.006)	$3.21^{+0.05}_{-0.04}$	$2.64^{+0.05}_{-0.04}$	0.269 (0.002)
Mean	0.112	1.99	1.34	0.343	1.98	1.22	0.299	2.78	2.05	0.253
Std Dev.	0.083	0.48	1.01	0.225	0.47	1.07	0.204	0.42	0.78	0.177
Median	0.087	1.89	1.65	0.334	1.95	1.56	0.271	2.77	2.20	0.218

Note. Units of luminosities are K km s^{-1} pc^2.

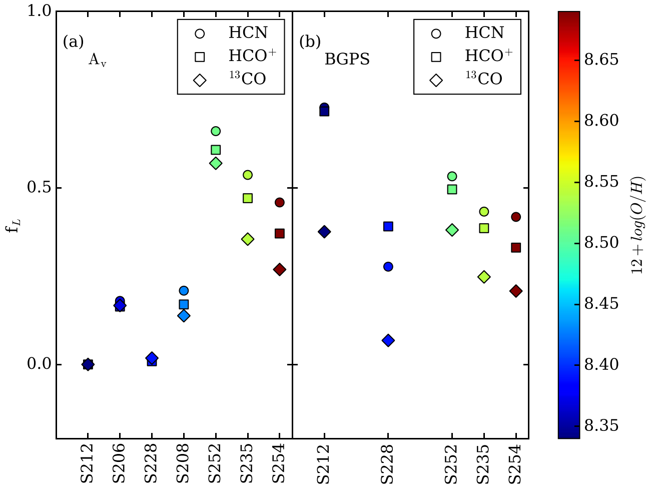

Figure 3. The fraction of luminosity (f_L) within the "in" region is plotted for each tracer vs. clouds. The f_L in the left panel is obtained from the $A_V \geqslant 8$ mag region, and in the right panel f_L is from the BGPS mask region. The targets are organized with increasing metallicity. Different symbols are used to separate the different tracers. Different colors indicate the metallicity of each source.

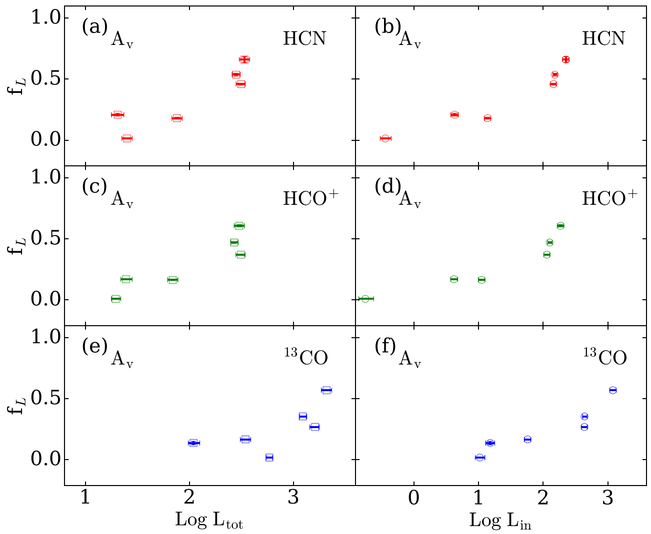

Figure 4. The fraction of line luminosity arising above $A_V \geqslant 8$ mag plotted vs. line luminosity. HCN is plotted in the top row, HCO$^+$ in the middle row, and ^{13}CO in the bottom row. The total line luminosities (Log L_{tot}) are on the left and luminosity from the "in" region (Log L_{in}) on the right.

inside the BGPS mask region ($N_{\mathrm{in}}/N_{\mathrm{tot}}$), the log of the total line luminosity (Log L_{tot}), the log of line luminosity arising from the BGPS "in" region (Log L_{in}), and the fractional luminosity ($f_L = L_{\mathrm{in}}/L_{\mathrm{tot}}$) in Table 3 for HCN, HCO$^+$, and ^{13}CO. The mean f_L values, listed in Table 3, are higher for HCN, followed by HCO$^+$ and ^{13}CO (see Figure 3b). Dense line tracers (HCN, HCO$^+$) show better agreement with BGPS emission than they did with the extinction criterion ($A_V \geqslant 8$ mag) for these five clouds having BGPS data.

The standard deviation of the f_L values is 0.149 and 0.137 for HCN and HCO$^+$, respectively, considerably lower than the values for the extinction criterion. Figure 5 shows the correlation between fractional line luminosity (f_L) arising from inside the BGPS mask region with LogL_{in} and total luminosity LogL_{tot}. The f_L values show no significant dependence on Log L_{tot} and Log L_{in} for any of the three tracers.

4.3. Conversion of Line Luminosity to Mass of Dense Gas

In this section, we measure the mass conversion factor for the outer Galaxy targets. The conversion factor is defined as the ratio between the mass of gas and line luminosities $M = \alpha_Q L_Q$, where the unit of α_Q is $M_\odot$ (K km s^{-1} pc^2)$^{-1}$. This conversion factor is used in extragalactic studies to estimate the mass of dense gas.

The dense gas mass of each source having BGPS data is estimated from its integrated flux density, $S_{1.1}$ (available in the BGPS source catalog table;[13] Rosolowsky et al. 2010), combined with distance (D) and dust temperature (T_{dust}). The 1.1 mm dust emission is assumed to be optically thin and at a single temperature, and a dust opacity is assumed:

$$M_{\mathrm{dense}} = \frac{S_{1.1} D^2 (\rho_g/\rho_d)}{B_\nu(T_{\mathrm{dust}})\,\kappa_{\mathrm{dust},1.1}}, \tag{7}$$

where B_ν is the Planck function evaluated at $\lambda = 1.1$ mm, $\kappa_{\mathrm{dust},1.1} = 1.14$ cm^2 g^{-1} is the dust opacity per gram of dust (Enoch et al. 2006), and gas-to-dust ratio (ρ_g/ρ_d) is assumed to be 100 (Hildebrand 1983). We use the relation after scaling it

---

[13] https://irsa.ipac.caltech.edu/data/BOLOCAM_GPS/tables/bgps_v2.1.tbl

Table 3
Line Luminosities versus BGPS Emission

Source	$N_{\rm in}/N_{\rm tot}$	Log $L_{\rm tot}$ HCN	Log $L_{\rm in}$ HCN	f_L HCN	Log $L_{\rm tot}$ HCO$^+$	Log $L_{\rm in}$ HCO$^+$	f_L HCO$^+$	Log $L_{\rm tot}$ ^{13}CO	Log $L_{\rm in}$ ^{13}CO	f_L ^{13}CO
S212	0.352	$1.89^{+0.15}_{-0.21}$	$1.75^{+0.15}_{-0.21}$	0.728 (0.045)	$1.95^{+0.15}_{-0.21}$	$1.80^{+0.15}_{-0.21}$	0.717 (0.025)	$2.49^{+0.15}_{-0.21}$	$2.06^{+0.15}_{-0.21}$	0.376 (0.017)
S228	0.049	$1.40^{+0.05}_{-0.05}$	$0.84^{+0.03}_{-0.03}$	0.277 (0.027)	$1.29^{+0.04}_{-0.05}$	$0.89^{+0.03}_{-0.03}$	0.391 (0.034)	$2.77^{+0.03}_{-0.03}$	$1.60^{+0.04}_{-0.04}$	0.068 (0.004)
S235	0.118	$2.45^{+0.04}_{-0.04}$	$2.08^{+0.03}_{-0.04}$	0.433 (0.009)	$2.43^{+0.03}_{-0.04}$	$2.02^{+0.03}_{-0.04}$	0.386 (0.006)	$3.09^{+0.03}_{-0.04}$	$2.49^{+0.03}_{-0.04}$	0.248 (0.001)
S252	0.165	$2.53^{+0.05}_{-0.05}$	$2.26^{+0.05}_{-0.05}$	0.533 (0.014)	$2.48^{+0.05}_{-0.05}$	$2.18^{+0.05}_{-0.05}$	0.496 (0.008)	$3.32^{+0.05}_{-0.05}$	$2.90^{+0.05}_{-0.05}$	0.381 (0.002)
S254	0.085	$2.50^{+0.05}_{-0.04}$	$2.12^{+0.05}_{-0.04}$	0.418 (0.007)	$2.49^{+0.05}_{-0.04}$	$2.01^{+0.05}_{-0.04}$	0.331 (0.005)	$3.21^{+0.05}_{-0.04}$	$2.53^{+0.05}_{-0.04}$	0.208 (0.001)
Mean	0.154	2.15	1.81	0.478	2.13	1.78	0.464	2.97	2.32	0.256
Std Dev.	0.106	0.44	0.51	0.149	0.46	0.46	0.137	0.31	0.50	0.116
Median	0.118	2.45	2.08	0.433	2.43	2.01	0.391	3.09	2.49	0.248

Note. Units of luminosities are K km s^{-1} pc^2.

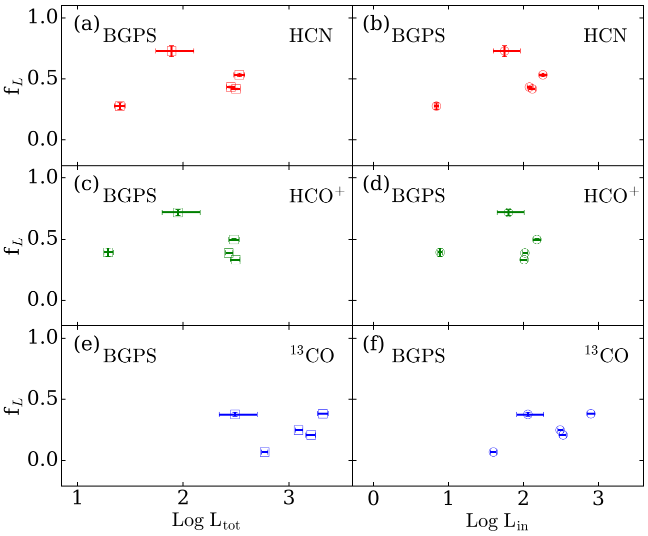

Figure 5. The fraction of line luminosity arising from the BGPS mask region plotted vs. line luminosity. HCN is plotted in the top row, HCO$^+$ in the middle row, and ^{13}CO in the bottom row. The total line luminosities (Log $L_{\rm tot}$) are on the left and luminosity from the "in" region (Log $L_{\rm in}$) on the right.

(Rosolowsky et al. 2010),

$$M_{\rm dense} = 13.1 M_\odot \left(\frac{D}{1\ {\rm kpc}}\right)^2 \left(\frac{S_{1.1}}{1 {\rm Jy}}\right) \left[\frac{e^{(13.0{\rm K}/T_{\rm dust})} - 1}{e^{(13.0/20)} - 1}\right]. \quad (8)$$

For consistency with Rosolowsky et al. (2010), we assume a single dust temperature ($T_{\rm dust} = 20$ K) for all sources to estimate the dense gas mass. For the sources with Herschel data, the derived $T_{\rm dust}$ is consistent with this choice. The values of dense mass ($M_{\rm dense}$) are listed in Table 4 in logarithmic scale. The uncertainties include distance uncertainties.

The mass conversion factor $\alpha_{\rm tot}$ is calculated as the mass of dense gas divided by the total luminosity of the clouds ($A_V > 1.5$ mag), where $\alpha_{\rm tot} = M_{\rm dense}/L_{\rm tot}$, and for $\alpha_{\rm in}$ the luminosity is restricted to the dense region based on the BGPS mask ($\alpha_{\rm in} = M_{\rm dense}/L_{\rm in}$). In Table 4, we list the conversion factors along with total line luminosities ($L_{\rm tot}$) and line luminosities inside the BGPS mask ($L_{\rm in}$) in logarithmic scale for HCN and HCO$^+$. We also estimated the statistical parameters (mean, standard deviation, and median) to understand the correlation between $M_{\rm dense}$ and the conversion factors ($\alpha_{\rm in}$, $\alpha_{\rm tot}$). The mean value of $\alpha_{\rm in}$ in logarithmic scale is $\langle {\rm Log}\ \alpha_{\rm in}({\rm HCN})\rangle = 1.28 \pm 0.08$, translating to $M_{\rm dense} = 19^{+3.8}_{-3.2} L_{\rm in}({\rm HCN})$, and for $\alpha_{\rm tot}$, $\langle {\rm Log}\ \alpha_{\rm tot}({\rm HCN})\rangle = 0.93 \pm 0.16$, translating to $M_{\rm dense} = 8.5^{+3.8}_{-2.6} L_{\rm tot}({\rm HCN})$. Our $\alpha_{\rm tot}$ value is close to the extragalactic conversion factor ($\alpha_{\rm HCN(1-0)} = 10$ $M_\odot$ (K km s^{-1} pc^2)$^{-1}$; Gao & Solomon 2004b), where luminosity from the whole cloud is considered to obtain mass. The $\alpha_{\rm in}$ value is similar to the value obtained by Wu (2010) for dense clumps. The theoretical prediction of α(HCN) by Onus et al. (2018) is 14 ± 6 $M_\odot$ (K km s^{-1} pc^2)$^{-1}$ for $n \geqslant 1 \times 10^4$ cm^{-3}, which corresponds to the dense gas of the cloud. Including the uncertainty, this theoretical value is consistent with either our $\alpha_{\rm in}$(HCN) or $\alpha_{\rm tot}$(HCN). Calculations for HCO$^+$ yield $\alpha_{\rm in} = 20.4^{+4.1}_{-3.4}$ $M_\odot$ (K km s^{-1} pc^2)$^{-1}$ and $\alpha_{\rm tot} = 9.1^{+3.2}_{-2.3}$ $M_\odot$ (K km s^{-1} pc^2)$^{-1}$, similar to the values for HCN.

Variation in $T_{\rm dust}$ by ±3 K produces changes in $\alpha_{\rm in}$ and $\alpha_{\rm tot}$ within the variation among sources, whereas variation by 5 K in dust temperature begins to produce changes outside that range. Higher $T_{\rm dust}$ of course produces lower values of $\alpha_{\rm in}$, $\alpha_{\rm tot}$; lower $T_{\rm dust}$ gives higher values.

We also estimate the mass of BGPS clumps from the Herschel-based column density maps from Marsh et al. (2017) for S228, S252, and S254. We use $M_{\rm dense} = \mu_{\rm H_2} m_{\rm H} A_{\rm pix} \sum N({\rm H_2})$, where mean molecular weight $\mu_{\rm H_2}$ is assumed to be 2.8 (Kauffmann et al. 2008), $m_{\rm H}$ is the mass of hydrogen, $A_{\rm pix}$ is the area of a pixel in cm^2, and $\sum N({\rm H_2})$ is the integrated column density. The mass values in logarithmic scale are 2.36, 4.09, and 3.72, respectively, for three targets. The values are higher than the BGPS mass measurement by an average of 0.34 in log scale, which is 2.2 in linear scale. The difference in the values is mainly caused by differing assumptions about the dust opacity. Marsh et al. (2017) used $\kappa(\lambda) = 0.1(\frac{\lambda}{300})^{-2}$ cm^2 g^{-1}, which implies a dust opacity per gram of dust at 1.1 mm of $\kappa_{1.1} = 0.74$ cm^2 g^{-1}, a value 1.5 times lower than the $\kappa_{\rm dust,1.1}$ value assumed in the BGPS mass measurement.

BGPS resolves out the extended structure of the clouds and gives a better measure of mean volume density of the dense regions than Herschel data. Our aim is to measure the L(HCN) in the mean high volume density region, not the column density region, for which Herschel works best.

4.4. Line Tracers versus Herschel Column Density

We also explore how well molecular lines trace the dust column density derived from Herschel data. Kauffmann et al. (2017) and Barnes et al. (2020) studied the relationship

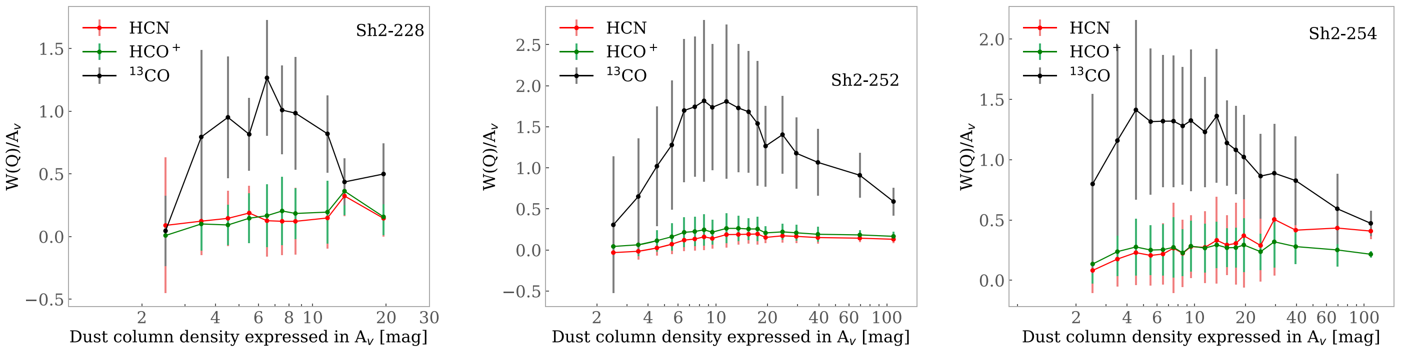

(a) (b) (c)

Figure 6. Line-to-mass ratio is plotted against A_V based on Herschel dust column density for the regions (a) S228, (b) S252, and (c) S254.

Table 4
$M_{\rm dense}$ versus Luminosities

Source	Log $M_{\rm dense}$ $M_\odot$	Log $L_{\rm tot}$ HCN	Log $L_{\rm in}$ HCN	Log α_{tot} HCN	Log $\alpha_{\rm in}$ HCN	Log $L_{\rm tot}$ HCO$^+$	Log $L_{\rm in}$ HCO$^+$	Log α_{tot} HCO$^+$	Log $\alpha_{\rm in}$ HCO$^+$
S212	$3.06^{+0.16}_{-0.25}$	$1.89^{+0.15}_{-0.21}$	$1.75^{+0.15}_{-0.21}$	1.17 ± 0.09	1.31 ± 0.08	$1.95^{+0.15}_{-0.21}$	$1.80^{+0.15}_{-0.21}$	1.11 ± 0.08	1.26 ± 0.08
S228	$2.19^{+0.07}_{-0.08}$	$1.40^{+0.05}_{-0.05}$	$0.84^{+0.03}_{-0.03}$	0.80 ± 0.07	1.35 ± 0.06	$1.29^{+0.04}_{-0.05}$	$0.89^{+0.03}_{-0.03}$	0.90 ± 0.07	1.31 ± 0.06
S235	$3.22^{+0.05}_{-0.05}$	$2.45^{+0.04}_{-0.04}$	$2.08^{+0.03}_{-0.04}$	0.77 ± 0.04	1.13 ± 0.03	$2.43^{+0.03}_{-0.04}$	$2.02^{+0.03}_{-0.04}$	0.79 ± 0.04	1.20 ± 0.03
S252	$3.53^{+0.06}_{-0.07}$	$2.53^{+0.05}_{-0.05}$	$2.26^{+0.05}_{-0.05}$	1.00 ± 0.04	1.28 ± 0.04	$2.48^{+0.05}_{-0.05}$	$2.18^{+0.05}_{-0.05}$	1.05 ± 0.04	1.35 ± 0.04
S254	$3.43^{+0.06}_{-0.06}$	$2.50^{+0.05}_{-0.04}$	$2.12^{+0.05}_{-0.04}$	0.93 ± 0.04	1.31 ± 0.04	$2.49^{+0.05}_{-0.04}$	$2.01^{+0.05}_{-0.04}$	0.93 ± 0.04	1.41 ± 0.04
Mean	3.09	2.15	1.81	0.93	1.28	2.13	1.78	0.96	1.31
Std Dev.	0.53	0.44	0.51	0.16	0.08	0.46	0.46	0.13	0.08
Median	3.22	2.45	2.08	0.93	1.31	2.43	2.01	0.93	1.31

Note. Units of luminosities are K km s^{-1} pc^2. Units of conversion factors are $M_\odot$ (K km s^{-1} pc^2)$^{-1}$.

between several molecular line emissions and dense gas in Orion A and W49 molecular clouds. The line-to-mass ratio is defined by $h_Q = W(Q)/A_V$, where $W(Q) = \int T_{mb} dv$ and $A_V \propto N(\mathrm{H_2})$. This ratio shows the relation between molecular line emission from transition Q and the mass reservoir characterized by A_V (Kauffmann et al. 2017). The factor h_Q is considered as a proxy for the line emissivity, or the efficiency of an emitting transition per H_2 molecule (Barnes et al. 2020).

We plot line-to-mass ratio (h_Q) versus extinction (A_V) based on Herschel column density for the three targets for which we have data (see Table 1). We have used the Herschel column density data from Marsh et al. (2017) for S228, S252, and S254 after regridding and convolving to TRAO maps' resolution and pixel size. Figure 6 shows how $W(Q)/A_V$ varies with increasing A_V obtained from dust-based column density. We exclude pixels with $A_V < 2$ mag because of observational uncertainties.

The line emissivity (h_Q) of ^{13}CO increases up to $A_V \approx$ 6–7 mag and then decreases gradually with increasing A_V, whereas for HCO$^+$ and HCN it does not decrease. ^{13}CO traces the diffuse part well but fails in high column density regions, where HCN and HCO$^+$ are more reliable. Both f_L and $W(Q)/A_V$ indicate that dense gas is traced best by HCN and HCO$^+$ but less well by ^{13}CO. Two possible reasons for ^{13}CO falling at high A_V are the following: (i) it becomes optically thick at high column densities, or (ii) if dust temperature falls below 20–25 K, ^{13}CO depletes on dust grains (Bergin & Langer 1997). Figure 7 explores the first reason by plotting the spectra of ^{13}CO and HCO$^+$ with increasing A_V for S254. HCO$^+$ continues to grow stronger with increasing column density, while ^{13}CO actually becomes somewhat weaker. Although no self-absorption features are prominent, the ^{13}CO line is likely optically thick. A similar effect has been seen in the other two targets as well. In principle, the optical depth is corrected for in the LTE model, but that model can fail if the excitation temperatures of ^{12}CO and ^{13}CO differ, as we discuss in Appendix C in more detail. Fortunately, the failure of ^{13}CO to trace column density mostly arises at $A_V > 8$ mag, so that our method using ^{13}CO to identify the dense regions is still valid.

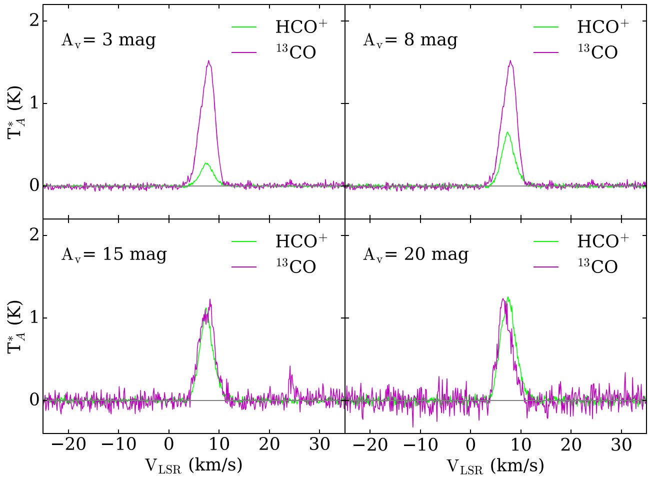

Figure 7. HCO$^+$ and ^{13}CO spectra are plotted for S254 with increasing A_V value for S254. ^{13}CO becomes optically thick in higher column densities.

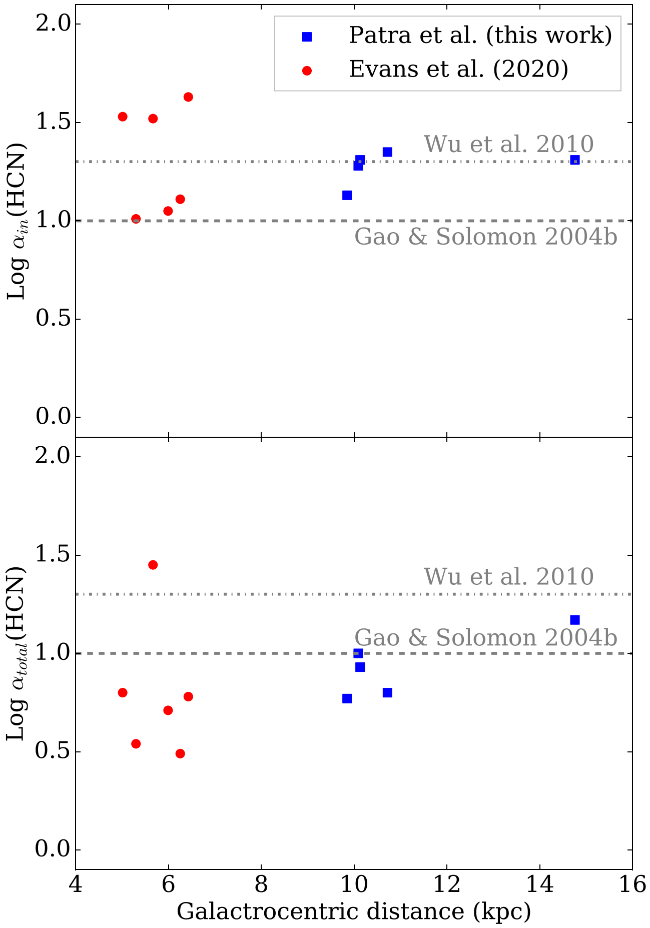

Figure 8. Variation of conversions factors Log $\alpha_{\rm in}$(HCN) and Log $\alpha_{\rm tot}$(HCN) for inner and outer Galaxy targets with Galactocentric distance (R_G).

5. Discussion

5.1. Comparison with Inner Galaxy Targets

A preliminary comparison between the outer and inner Galaxy targets can provide hints about the effects of Galactic environment. In their study of six inner Galaxy clouds with HCN and HCO$^+$ ($J = 1 \rightarrow 0$), Evans et al. (2020) found a significant amount of luminosity from the diffuse part of the clouds. That is also true for the outer Galaxy clouds, but the fraction of luminosity arising inside the $A_V \geqslant 8$ mag or the BGPS region is larger in the outer Galaxy clouds. In addition, the behaviors of individual tracers differ in both regimes. For inner Galaxy clouds, the average ratio $\langle f_{\rm L}({\rm HCO^+})/f_{\rm L}({\rm HCN})\rangle = 1.14 \pm 0.18$ for the $A_V \geqslant 8$ mag criterion compared to 0.83 ± 0.10 for the outer Galaxy clouds. For inner Galaxy clouds f_L(HCO$^+$) is greater than f_L(HCN), but for the outer Galaxy the order is opposite.

Evans et al. (2020) also calculated the conversion factor between $M_{\rm dense}$ measured by millimeter-wave continuum data and luminosity coming from the dense region. For inner Galaxy clouds $\alpha_{\rm in}$(HCN) is 20^{+16}_{-9} $M_\odot$ (K km s^{-1} pc^2)$^{-1}$, whereas it is $19^{+3.8}_{-3.2}$ $M_\odot$ (K km s^{-1} pc^2)$^{-1}$ for outer Galaxy clouds. Considering the whole cloud, the mass–luminosity conversion factor, $\alpha_{\rm tot}$(HCN), was $6.2^{+6.6}_{-3.0}$ $M_\odot$ (K km s^{-1} pc^2)$^{-1}$ for inner Galaxy clouds and $8.5^{+3.8}_{-2.6}$ $M_\odot$ (K km s^{-1} pc^2)$^{-1}$ for outer Galaxy clouds. From the above values, we can see that $\alpha_{\rm tot}$ and $\alpha_{\rm in}$ for outer Galaxy clouds are consistent with inner Galaxy values. Figure 8 shows the variation of conversion factors with R_G for both sets of targets. However, the mean density probed depends on heliocentric distance, and the inner Galaxy clouds are on average farther away. The high outlier in the bottom panel of Figure 8 is an inner Galaxy cloud that had very strong self-absorption in HCN, lowering the line luminosity and raising $\alpha_{\rm tot}$(HCN). Bigger samples are needed to understand all the effects.

5.2. Potential Impact of Metallicity on Fractional Luminosity?

HCN and HCO$^+$ are linear molecules with large dipole moments and similar energy levels, but differing in the elemental compositions (N vs. O). This difference in chemical structure makes them sensitive to the chemistry of the ISM. Hence, we can expect a connection between the abundance ratio of N/O and HCN/HCO$^+$ (Braine et al. 2017). The ratio of total luminosities, $L({\rm HCO^+})/L({\rm HCN})$, averaged in the logs, is 0.98 for outer Galaxy clouds, while this factor is 0.56 for inner Galaxy targets (Evans et al. 2020). The higher value in the outer Galaxy is consistent with the extragalactic studies on low-metallicity systems (1.8–3, LMC, SMC, Chin et al. 1997; Galametz et al. 2020; 1.1–2.8, IC 10, Nishimura et al. 2016; Braine et al. 2017; Kepley et al. 2018; 1.1–2.5, M33, Buchbender et al. 2013; Braine et al. 2017; 1.2, M31, Brouillet et al. 2005). Hence, in the low-metallicity environments HCO$^+$ is as luminous as HCN but less concentrated in dense regions compared to high-metallicity regions.

The f_L values based on A_V analysis increase with the metallicity (Figure 3), but f_L values based on BGPS analysis do not. A possible reason for this difference is that we use the [^{12}CO]/[^{13}CO] ratio in the derivation of the molecular hydrogen column density (N(H$_2$)) map (Section 4.1), which is a function of R_G and indirectly related to metallicity. For BGPS, the same opacity value is used regardless of metallicity, so the metallicity effect is not incorporated there. This study hints at interesting trends with the Galactic environment and indicates the need for a larger sample to study it further.

6. Conclusions

In this paper, we study seven outer Galaxy star-forming regions with HCN and HCO$^+$ $J = 1 \rightarrow 0$ transitions obtained from the TRAO 14 m telescope and compare these dense line tracers with extinction, 1.1 mm thermal dust continuum emission (BGPS), and dust column density from Herschel. The results are summarized below.

1. The luminosity coming from the "dense" region based on extinction criteria and BGPS mask maps (indicated as "in") is prominent for most of the clouds, but there are significant amounts of luminosity coming from outside the "dense" region (indicated as "out") for most of the clouds. The fraction of the total line luminosity arising from the dense region, as indicated by both the BGPS and extinction maps, is higher in HCN, followed by HCO$^+$ and ^{13}CO. The HCN emission is generally less extended than the HCO$^+$ emission.
2. In the outer Galaxy, HCO$^+$ is as luminous as HCN, but HCO$^+$ is less concentrated in the dense regions; these are the opposite of the trends in the inner Galaxy.
3. Both HCN and HCO$^+$ show better agreement with millimeter continuum emission than they do with the extinction criterion for the clouds having BGPS data. The

dense line tracers in S212 and S228 do not agree with the extinction criterion.

4. The fraction of line luminosity arising from the dense region based on extinction criterion increases with metallicity, but there is no such variation for the analysis based on millimeter continuum (Figure 3). For lower-metallicity targets, the fractions of the luminosity of the three tracers (HCN, HCO^+, and ^{13}CO) arising in high-extinction regions are comparable, but all are low.
5. For five clouds, we estimate the mass conversion factor (α_{in}) between dense gas mass (M_{dense}) arising from the BGPS mask region and the line luminosities of HCN and HCO^+, both within that region (α_{in}) and for the whole cloud (α_{tot}) in Section 4.3. The α_{tot} value is consistent with the literature value used in extragalactic studies (10 $M_\odot$ (K km s^{-1} $pc^2)^{-1}$; Gao & Solomon 2004b), while the α_{in} value is consistent with those found in studies of dense Galactic clumps (Wu 2010). In addition, the theoretical value obtained by Onus et al. (2018) for HCN is consistent with either our α_{in}(HCN) or α_{tot}(HCN).
6. We measure the line-to-mass ratio ($W(Q)/A_V$) for the three targets (S228, S252, and S254) with column densities from Herschel (Section 4.4). The ^{13}CO traces column density well over the range $A_V = 4$–10 mag, but HCN and HCO^+ trace it better for higher A_V, confirming the view that dense line tracers (HCN and HCO^+) are more sensitive to the high column density regions than is ^{13}CO.

The authors thank the referee for constructive comments that improved the clarity of the paper. We thank the staff of the TRAO for support during the course of these observations. S.P. thanks DST-INSPIRE Fellowship (No. IF180092) of the Department of Science and Technology to support the Ph.D. program. N.J.E. thanks the Department of Astronomy at the University of Texas at Austin for ongoing research support. K.-T.K. is supported by the Korea Astronomy and Space Science Institute grant funded by the Korea government (MSIT; Project No. 2022-1-840-05). We are grateful to Adam Ginsburg for sharing information on BGPS.

Facilities: TRAO 14 m Telescope, FCRAO, BGPS, *Herschel. Software:* astropy (Astropy Collaboration et al. 2013, 2018; The Astropy Collaboration et al. 2022), numpy (van der Walt et al. 2011), matplotlib (Hunter 2007), GILDAS (Pety 2018), DS9 (Joye & Mandel 2003; Smithsonian Astrophysical Observatory 2000).

Appendix A
Target Details

All of the sources were identified in the second catalog of visible H II regions by Sharpless (1959).

A1. Sh2-206

Sh2-206 (hereafter S206) was mapped with the center position $l = 150.5886$, $b = -0.8570$ with a map size $15' \times 15'$. This H II region is not excited by a cluster, but by a single massive star BD +50886 (Georgelin et al. 1973). An ionization front forms the bright central region of this target, and it surrounds the O4V exciting star to the south and west (Deharveng et al. 2000). The heliocentric distance of this region is $2.96^{+0.17}_{-0.15}$ kpc, measured from the parallax information of the massive star, and the Galactocentric distance is $R_G = 10.88^{+0.25}_{-0.26}$ kpc (Méndez-Delgado et al. 2022).

We use the velocity range −27 to −19 km s^{-1} to produce the column density map from ^{13}CO and integrated intensity map for HCO^+. For HCN we use the velocity range −34 to −14 km s^{-1} for the HCN integrated intensity map. The presence of a dense region ($A_V \geqslant 8$ mag) is indicated with the white contour on top of the integrated intensity of HCN and HCO^+ in Figure 1 (S206). There is strong detection of HCN and HCO^+ emission in both "in" and "out" regions for extinction in the spectrum plots (Figure 2(a)). The f_L value based on A_V analysis is higher for HCN, followed by ^{13}CO and HCO^+. This target lacks data in millimeter-wave continuum and Herschel.

A2. Sh2-208

Sh2-208 (hereafter S208) was mapped with center position $l = 151.3098$, $b = 1.9045$ with a map size $10' \times 20'$. This H II region is located at a heliocentric distance of $4.02^{-0.25}_{+0.27}$ kpc in an interarm island between the Cygnus and Perseus arms (Yasui et al. 2016), and the corresponding Galactocentric distance is $11.87^{-0.34}_{+0.37}$ kpc. This H II region is located in a sequential star-forming region, and the probable dominant star is GSC 03719 −00517 (Yasui et al. 2016).

We use the velocity range −32 to −28 km s^{-1} to produce the column density map from ^{13}CO and integrated intensity map for HCO^+. For HCN we use the velocity range −40 to −23 km s^{-1} for the integrated intensity map. Figure 1 shows the integrated intensity plot of HCN and HCO^+, and the white contours show the area above $A_V = 8$ mag. The extinction criterion of dense gas is in good agreement with the emission of HCN and HCO^+. Figure 1 (S208) shows that strong emission is coming from the "in" region for both lines.

A3. Sh2-212

Sh2-212 (hereafter S212) is a bright optically visible H II region, ionized by a cluster (NGC 1624) containing an O7-type star. S212 appears circular in the optical band around the central cluster. The molecular cloud appears as a semicircular shape in the southern part of the region. The region contains multiple substructures and indicates that it is evolving in a nonhomogeneous medium (Deharveng et al. 2008). This region is a likely example of the collect-and-collapse process triggering massive star formation (see Deharveng et al. 2008; Jose et al. 2011, for details).

Our map covered a region of $13' \times 14'$ centered on $l = 155.3375$, $b = 2.6345$. This target lies ∼300 pc above the Galactic plane. The heliocentric distance is $6.65^{-1.26}_{+1.36}$ kpc (Méndez-Delgado et al. 2022). This target has the highest Galactocentric distance (14.76 ± 1.30 kpc) in the sample and the lowest metallicity.

To derive the column density map from ^{13}CO and for the integrated intensity map of HCO^+, we use the velocity integration range −39 to −30.5 km s^{-1}. For HCN we use the velocity range −44 to −26 km s^{-1} for the integrated intensity map. Figure 1 (S212) shows the integrated intensity plots of HCN and HCO^+. For this target there is no region with $A_V \geqslant 8$ mag, so there is no white contour present in the figure. But the positions of the BGPS mask (shown in black contours) and HCN and HCO^+ show good agreement. Figure 2(c) shows the spectra for both extinction- and BGPS-based analysis.

A4. Sh2-228

Sh2-228 (hereafter S228) was mapped in Galactic coordinates with the center position $l = 169.1432$, $b = -1.0475$ with a map size $11' \times 33'$. This H II region is located on the Perseus arm near the large Auriga OB1 association. It is a vast region in which star formation is active. A young cluster IRAS 05100 +3723 is associated with the H II region S228 (Yadav et al. 2022). The heliocentric distance of this target is 2.56 ± 0.09 kpc, and the corresponding Galactocentric distance $R_G = 10.72 \pm 0.19$ kpc.

To derive the column density map from ^{13}CO and for the integrated intensity map of HCO$^+$, we use the velocity integration range -12 to -3.5 km s^{-1}. For HCN we use the velocity range -16 to 2 km s^{-1} for the integrated intensity map. Figure 1 (S228) shows the position of the $A_V \geqslant 8$ mag region and BGPS clump positions with white and black contours, respectively, on the integrated intensity maps of HCN and HCO$^+$. The emission of HCN and HCO$^+$ shows good agreement with the BGPS position, but there is no strong emission from HCN and HCO$^+$ in the $A_V \geqslant 8$ mag region (see spectra in Figure 2(d)). The lines of ^{13}CO in the region of the BGPS peak are slightly below the value corresponding to $A_V = 8$, instead indicating $A_V = 6$ or 7 mag. There are two peaks in the Herschel column density maps, one at the position of the BGPS clump and the other below the region where ^{13}CO peaks. The lack of strong ^{13}CO emission at a peak of BGPS, HCN, and HCO$^+$ is unusual. We examined the spectra of ^{13}CO at the BGPS peak for evidence of self-absorption, but none was obvious. The f_L value based on BGPS analysis is higher for HCN, followed by HCO$^+$ and ^{13}CO. The line-to-mass ratio versus dust-based extinction plot (Figure 6(a)) shows that HCO$^+$ and HCN are better tracers in the dense region than ^{13}CO.

A5. Sh2-235

Sh2-235 (hereafter S235) is an extended H II region with active star formation and is located in the Perseus spiral arm (Heyer et al. 1996). This star-forming region consists of "S235main" and S235A, S235B, and S235C regions (hereafter "S235ABC"; Dewangan & Anandarao 2011). A single massive star BD +351201 of O9.5V type is ionizing "S235main," while the compact H II regions in "S235ABC" are excited by B1V −B0.5V stars (Chavarria et al. 2014; Dewangan & Ojha 2017, and references therein). This cloud has two velocity components, "S235main" with velocity range -24 to -18 km s^{-1} and "S235ABC" with velocity range -18 to -13 km s^{-1}. These two clouds are interconnected by a bridge feature with less intensity (Evans & Blair 1981; Dewangan & Ojha 2017). This region is also known for the star formation activities influenced by the cloud−cloud collision mechanism (Dewangan & Ojha 2017).

We mapped a $30' \times 30'$ region with the center $l = 173.6682$, $b = 2.7799$. The heliocentric distance is 1.66 ± 0.07 kpc, derived from the parallax information of the ionizing star BD +351201 from Gaia EDR3 data. The corresponding Galactocentric distance $R_G = 9.85^{-0.17}_{+0.16}$ kpc (Méndez-Delgado et al. 2022).

To derive the column density map from ^{13}CO and for the integrated intensity map of HCO$^+$, we use the velocity integration range -24.5 to -12 km s^{-1}. For HCN we use the velocity range -32 to -7 km s^{-1} for the integrated intensity map. The two velocity components at -20 and -17.3 km s^{-1} are not separable at some positions, so the integration range we consider covers both the components. All the tracers (HCN, HCO$^+$, extinction, and BGPS emission) agree with each other (Figure 1 (S235)). The white contour ($A_V \geqslant 8$ mag) covers a larger area than the BGPS region (black contours). There are strong detections of HCN and HCO$^+$ emission in both "in" and "out" regions for extinction and BGPS in the spectrum plots (Figure 2(e)).

A6. Sh2-252

Sh2-252 (hereafter S252), also known as NGC 2175, is an optically bright, evolved H II region with size ~20 pc. This region is part of the Gemini OB1 association. The central star HD 42088 of spectral type O6.5 V is the main ionizing source (Jose et al. 2012). This region also contains four compact H II (CH II) regions (A, B, C, and E; Felli et al. 1977) and is powered by ionizing sources with spectral type later than O6.5V in each of them. This cloud has several regions of recent star formation activity.

Table 4 of Jose et al. (2012) listed the massive stars in each of these clumps with their spectral types. We take the parallax information of those stars (ID 1–6 and 11–12 from Table 4 of Jose et al. 2012) from Gaia EDR3 and calculate the distance by averaging all the parallaxes. The distance is $1.92^{+0.12}_{-0.11}$ kpc, and the corresponding Galactocentric distance $R_G = 10.09^{-0.11}_{+0.12}$ kpc. This source was mapped with center position $l = 189.8418$, $b = 0.3156$ with a map size $30' \times 30'$.

We use the velocity range 2–14 km s^{-1} to produce the column density map from ^{13}CO and the integrated intensity map of HCO$^+$. For HCN we use the velocity range -4 to 20 km s^{-1} for integrated intensity map. Figure 1 (S252) shows the contour of $A_V \geqslant 8$ mag (in white) and BGPS clumps (in black) in the integrated intensity maps of HCN and HCO$^+$, and all the tracers are in good agreement. There is strong detection of HCN and HCO$^+$ emission in both "in" and "out" regions for extinction and BGPS in the spectrum plots (Figure 2(f)).

A7. Sh2-254 Complex

This region is a complex with five H II regions (Sh2-254, Sh2-255, Sh2-256, Sh2-257, and Sh2-258) and part of the Gemini OB association. This is a sequential star-forming region triggered by expanding H II regions (Bieging et al. 2007; Chavarría et al. 2008; Ojha et al. 2011). These five evolved H II regions are projected on a 20 pc long filament. The exciting stars present in S254, S255, S256, S257, and S258 have spectral types of O9.6V, B0.0V, B0.9V, B0.5V, and B1.5V, respectively (Chavarría et al. 2008). Ladeyschikov et al. (2021) studied the link between the gas−dust constituents and the YSO distribution. They identified high-density gas (HCO$^+$ ($J = 1 \rightarrow 0$) and CS ($J = 2 \rightarrow 1$)) in the interclump bridge position between the star clusters S255N and S256-south and suggested that the clusters have an evolutionary link. We mapped a $50' \times 34'$ area of the Sh2-254 complex with the center position $l = 192.7935$, $b = 0.0290$. The Galactocentric distance is $R_G = 10.13 \pm 0.21$ kpc, and the heliocentric distance is $1.96^{-0.09}_{+0.12}$ kpc based on GAIA EDR3 (Méndez-Delgado et al. 2022).

We use the velocity range 4.5–11.5 km s^{-1} to produce the column density map from ^{13}CO and the integrated intensity map of HCO$^+$. For HCN we use the velocity range −4 to 17 km s^{-1} for the integrated intensity map. The contour plot (Figure 1 (S254)) for this cloud shows good agreement among HCN, HCO$^+$, extinction, and BGPS. There are strong detections of HCN and HCO$^+$ emission in both "in" and "out" regions for extinction and BGPS in the spectrum plots (Figure 2(g)).

Appendix B
Reduction Details

Our standard procedure of data reduction is as follows. First, we check the data to find the velocity intervals with significant emission ($v_{\rm win}$). Then, we exclude the window of velocity having emission while removing a baseline order, also using only enough velocity range to get a good baseline on each end ($v_{\rm sp}$). After that, we made spectral cubes in FITS format for further analysis. The values of the total velocity range and excluded windows are shown in Table B1. We experimented on the velocity range ($v_{\rm sp}$) and baseline order to get the best fit.

Change in baseline order.—First, we have experimented on the baseline order removal. For a same target, by keeping $v_{\rm win}$ and $v_{\rm sp}$ the same, we tried both first- and second-order baselines. For most of the cases, the second-order baseline removal was superior.

Change in v_{sp} range.—Further, we change the velocity range of $v_{\rm sp}$ (while keeping the baseline removal order fixed) for each target with two different sets, (i) *wider range of v_{sp}* and (ii) *narrow range of v_{sp}*, to see the effect on final results.

In the final analysis, we used baselines of order 2 with a wider range of $v_{\rm sp}$. Table B1 shows the choice of velocity ranges and lists the positions of all the peaks in terms of offset from the center of the map, with offsets in Galactic coordinates.

Table B1
Data Reduction Details

Source	Line	$v_{\rm sp}$ (km s^{-1})	$v_{\rm win}$ (km s^{-1})	Peak Offset (arcsec)	Notes
S206	HCN	−45, 0	−32, −14	280, 280	Peak position 1
S206	HCO$^+$	−45, 0	−27, −19	280, 280	Peak position 1
S206	HCN	−45, 0	−32, −14	180, 120	Peak position 2
S206	HCO$^+$	−45, 0	−27, −19	180, 120	Peak position 2
S206	HCN	−45, 0	−32, −14	−40, −280	Peak position 3
S206	HCO$^+$	−45, 0	−27, −19	−40, −280	Peak position 3
S208	HCN	−55, −5	−40, −23	−100, 200	
S208	HCO$^+$	−55, −5	−34, −27	−100, 200	
S212	HCN	−60, −10	−44, −26	0, −160	Peak position 1
S212	HCO$^+$	−60, −10	−40, −29	0, −160	Peak position 1
S212	HCN	−60, −10	−44, −26	120, −40	Peak position 2
S212	HCO$^+$	−60, −10	−40, −29	120, −40	Peak position 2
S228	HCN	−30, 20	−16, 3	160, 520	
S228	HCO$^+$	−30, 20	−11, −2	160, 520	
S235	HCN	−50, 10	−32, −7	−160, 100	Peak position 1
S235	HCO$^+$	−50, 10	−26, −12	−160, 100	Peak position 1
S235	HCN	−50, 10	−32, −7	180, −300	Peak position 2
S235	HCO$^+$	−50, 10	−26, −12	180, −300	Peak position 2
S235	HCN	−50, 10	−32, −7	0, 340	Peak position 3
S235	HCO$^+$	−50, 10	−26, −12	0, 340	Peak position 3
S235	HCN	−50, 10	−32, −7	−180, 360	Peak position 4
S235	HCO$^+$	−50, 10	−26, −12	−180, 360	Peak position 4
S252	HCN	−20, 40	−4, 18	−220, 100	Peak position 1
S252	HCO$^+$	−20, 40	2, 14	−220, 100	Peak position 1
S252	HCN	−20, 40	−4, 20	−120, 120	Peak position 2
S252	HCO$^+$	−20, 40	0, 15	−120, 120	Peak position 2
S252	HCN	−20, 40	−4, 20	400, 60	Peak position 3
S252	HCO$^+$	−20, 40	0, 15	400, 60	Peak position 3
S252	HCN	−20, 40	−4, 20	0, 640	Peak position 4
S252	HCO$^+$	−20, 40	0, 15	0, 640	Peak position 4
S252	HCN	−20, 40	−4, 20	400, −300	Peak position 5
S252	HCO$^+$	−20, 40	0, 15	400, −300	Peak position 5
S252	HCN	−20, 40	−4, 20	−620, −520	Peak position 6
S252	HCO$^+$	−20, 40	0, 15	−620, −520	Peak position 6
S254	HCN	−25, 35	−4, 17	−720, −280	Peak position 1
S254	HCO$^+$	−25, 35	2, 14	−720, −280	Peak position 1
S254	HCN	−25, 35	−4, 17	740, 360	Peak position 2
S254	HCO$^+$	−25, 35	2, 14	740, 360	Peak position 2
S254	HCN	−25, 35	−4, 17	−120, 240	Peak position 3
S254	HCO$^+$	−25, 35	2, 14	−120, 240	Peak position 3
S254	HCN	−25, 35	−4, 17	220, 280	Peak position 4
S254	HCO$^+$	−25, 35	2, 14	220, 280	Peak position 4

Appendix C
The H_2 Column Density Map Derived from ^{12}CO and ^{13}CO

To measure the molecular hydrogen (H_2) column density map from ^{12}CO and ^{13}CO, we assume that both the molecular lines arise from the same region of the clouds. We follow the steps from Ripple et al. (2013) and Pineda et al. (2010). The ^{12}CO line is optically thick, and its isotopologue ^{13}CO is optically thin. We assume that they both have the same excitation temperature ($T_{\rm ex}$). Hence, we derive the $T_{\rm ex}$ using the peak brightness temperature ($T_{\rm 12,pk}$) of the optically thick ^{12}CO line:

$$T_{\rm ex} = \frac{5.53}{\ln\left(1 + \frac{5.53}{T_{\rm 12,pk} + 0.83}\right)}. \quad ({\rm C1})$$

We derive the optical depth of ^{13}CO in the upper rotational state ($J = 1$), $\tau_{13,1}$, using the main-beam brightness temperature of ^{13}CO, T_{13}, and substitute $T_{\rm ex}$ derived from the ^{12}CO observations into the following equation:

$$\tau_{13,1}(v) = -\ln\left[1 - \frac{T_{13}(v)}{5.29}([\exp(5.29/T_{\rm ex}) - 1]^{-1} - 0.16)^{-1}\right]. \quad ({\rm C2})$$

The optical depth in ^{13}CO is then converted into an upper-level column density as follows:

$$N_U = \frac{8\pi k\nu^2}{hc^3 A_{UL}\, C(T_{\rm ex})}\left[\frac{\int \tau_{13,1}(v)dv}{\int(1 - \exp(-\tau_{13,1}(v)))dv}\right]\int T_{13}(v)dv, \quad ({\rm C3})$$

where A_{UL} is the Einstein A-coefficient and ν is the frequency of the $J = 1 \rightarrow 0$ transition. Here we incorporated the correction factor $C(T_{\rm ex}) = \left(1 - \frac{e^{T_0/T_{\rm ex}} - 1}{e^{T_0/T_{\rm bg}} - 1}\right)$, which is equal to unity in the limit $T_{\rm bg} \rightarrow 0$.

The column density of the upper level ($J = 1$) is related to the total ^{13}CO column density by the following equation:

$$N_{^{13}\rm CO} = N_U \frac{Z}{2J + 1}\exp[hB_0 J(J + 1)/kT_{\rm ex}]. \quad ({\rm C4})$$

To calculate the upper-level column density, we use the rotational constant for ^{13}CO, $B_0 = 5.51 \times 10^{10}$ s^{-1}, and use the partition function Z, which is defined as

$$Z = \sum_{J=0}^{\infty}(2J + 1)\exp[-hB_0 J(J + 1)/kT_{\rm ex}]. \quad ({\rm C5})$$

This equation using a single $T_{\rm ex}$ assumes that all levels have the same $T_{\rm ex}$ (the so-called LTE approximation).

The assumption that $T_{\rm ex}$ is the same for ^{13}CO and ^{12}CO (in Equation (C1)) can fail. If the excitation temperature of ^{13}CO is higher (lower) than that of ^{12}CO, the optical depth of ^{13}CO will be overestimated (underestimated) when the $T_{\rm ex}$ from ^{12}CO is used in Equation (C2). For clouds heated from the outside by hot stars, the front of the cloud is likely to be hotter than the inside, leading to an underestimate of the optical depth of ^{13}CO.

Roueff et al. (2021) checked the validity of the simple assumption of equal $T_{\rm ex}$ in the Orion B molecular cloud by using the Cramer–Rao Bound (CRB) technique to estimate different physical properties (column density, excitation temperature, velocity dispersion, etc.) in the framework of LTE radiative transfer model. They found that isotopologues had different excitation temperatures: ^{12}CO (30 K) had higher $T_{\rm ex}$ than ^{13}CO (17 K), so that $T_{\rm ex}(^{12}{\rm CO})/T_{\rm ex}(^{13}{\rm CO}) \sim 1.7$. If a similar situation applies to the more opaque parts of our clouds, ^{13}CO is likely to underestimate the column density.

ORCID iDs

Sudeshna Patra https://orcid.org/0000-0002-3577-6488
Neal J. Evans II https://orcid.org/0000-0001-5175-1777
Kee-Tae Kim https://orcid.org/0000-0003-2412-7092
Mark Heyer https://orcid.org/0000-0002-3871-010X
Jens Kauffmann https://orcid.org/0000-0002-5094-6393
Jessy Jose https://orcid.org/0000-0003-4908-4404
Manash R. Samal https://orcid.org/0000-0002-9431-6297
Swagat R. Das https://orcid.org/0000-0001-7151-0882

References

Astropy Collaboration, Price-Whelan, A. M., Sipőcz, B. M., et al. 2018, AJ, 156, 123
Astropy Collaboration, Robitaille, T. P., Tollerud, E. J., et al. 2013, A&A, 558, A33
The Astropy Collaboration, Price-Whelan, A. M., Lian Lim, P., et al. 2022, ApJ, 935, 167
Balser, D. S., Rood, R. T., Bania, T. M., & Anderson, L. D. 2011, ApJ, 738, 27
Barnes, A. T., Kauffmann, J., Bigiel, F., et al. 2020, MNRAS, 497, 1972
Bergin, E. A., & Langer, W. D. 1997, ApJ, 486, 316
Bieging, J. H., Peters, W. L., Vilaro, B. V., Schlottman, K., & Kulesa, C. 2007, in Triggered Star Formation in a Turbulent ISM, ed. B. G. Elmegreen & J. Palous, Vol. 237 (Cambridge: Cambridge Univ. Press), 396
Bolatto, A. D., Wolfire, M., & Leroy, A. K. 2013, ARA&A, 51, 207
Braine, J., Shimajiri, Y., André, P., et al. 2017, A&A, 597, A44
Brouillet, N., Muller, S., Herpin, F., Braine, J., & Jacq, T. 2005, A&A, 429, 153
Buchbender, C., Kramer, C., Gonzalez-Garcia, M., et al. 2013, A&A, 549, A17
Chavarria, L., Allen, L., Brunt, C., et al. 2014, MNRAS, 439, 3719
Chavarría, L. A., Allen, L. E., Hora, J. L., Brunt, C. M., & Fazio, G. G. 2008, ApJ, 682, 445
Chin, Y. N., Henkel, C., Whiteoak, J. B., et al. 1997, A&A, 317, 548
Chini, R., & Wink, J. 1984, A&A, 139, L5
Deharveng, L., Lefloch, B., Kurtz, S., et al. 2008, A&A, 482, 585
Deharveng, L., Pena, M., Caplan, J., & Costero, R. 2000, MNRAS, 311, 329
Dewangan, L. K., & Anandarao, B. G. 2011, MNRAS, 414, 1526
Dewangan, L. K., & Ojha, D. K. 2017, ApJ, 849, 65
Dunham, M. K., Rosolowsky, E., Evans, N. J. I., Cyganowski, C., & Urquhart, J. S. 2011, ApJ, 741, 110
Enoch, M. L., Young, K. E., Glenn, J., et al. 2006, ApJ, 638, 293
Esteban, C., Fang, X., Garcia-Rojas, J., & Toribio San Cipriano, L. 2017, MNRAS, 471, 987
Esteban, C., & Garcia-Rojas, J. 2018, MNRAS, 478, 2315
Evans, N. J. I. 1989, RMxAA, 18, 21
Evans, N. J. I. 1999, ARA&A, 37, 311
Evans, N. J. I., & Blair, G. N. 1981, ApJ, 246, 394
Evans, N. J. I., Heiderman, A., & Vutisalchavakul, N. 2014, ApJ, 782, 114
Evans, N. J. I., Kim, K. T., Wu, J., et al. 2020, ApJ, 894, 103
Felli, M., Habing, H., & Israel, F. 1977, A&A, 59, 43
Galametz, M., Schruba, A., De Breuck, C., et al. 2020, A&A, 643, A63
Gao, Y., & Solomon, P. M. 2004a, ApJ, 606, 271
Gao, Y., & Solomon, P. M. 2004b, ApJS, 152, 63
Georgelin, Y., Georgelin, Y., & Roux, S. 1973, A&A, 25, 337
Ginsburg, A., Glenn, J., Rosolowsky, E., et al. 2013, ApJS, 208, 14
Gravity Collaboration, Abuter, R., Amorim, A., et al. 2019, A&A, 625, L10
Heiderman, A., Evans, N. J. I., Allen, L. E., Huard, T., & Heyer, M. 2010, ApJ, 723, 1019
Heyer, M., Gregg, B., Calzetti, D., et al. 2022, ApJ, 930, 170
Heyer, M. H., Carpenter, J. M., & Ladd, E. F. 1996, ApJ, 463, 630
Hildebrand, R. H. 1983, QJRAS, 24, 267
Hunter, John D. 2007, CSE, 9, 90
Jacob, A. M., Menten, K. M., Wiesemeyer, H., et al. 2020, A&A, 640, A125
Jeong, I.-G., Kang, H., Jung, J., et al. 2019, JKAS, 52, 227
Jiménez-Donaire, M. J., Bigiel, F., Leroy, A. K., et al. 2019, ApJ, 880, 127
Jose, Jessy, Pandey, A. K., Ogura, K., et al. 2011, MNRAS, 411, 2530
Jose, J., Pandey, A. K., Ogura, K., et al. 2012, MNRAS, 424, 2486

Joye, W. A., & Mandel, E. 2003, in ASP Conf. Ser. 295, Astronomical Data Analysis Software and Systems XII, ed. H. E. Payne, R. I. Jedrzejewski, & R. N. Hook (San Francisco, CA: ASP), 489
Kauffmann, J., Bertoldi, F., Bourke, T. L., Evans, N. J. I., & Lee, C. W. 2008, A&A, 487, 993
Kauffmann, J., Goldsmith, P. F., Melnick, G., et al. 2017, A&A, 605, L5
Kennicutt, R. C., & Evans, N. J. 2012, ARA&A, 50, 531
Kepley, A. A., Bittle, L., Leroy, A. K., et al. 2018, ApJ, 862, 120
Lacy, J. H., Sneden, C., Kim, H., & Jaffe, D. T. 2017, AAS Meeting, 230, 215.02
Lada, C. J., Forbrich, J., Lombardi, M., & Alves, J. F. 2012, ApJ, 745, 190
Lada, C. J., Lombardi, M., & Alves, J. F. 2010, ApJ, 724, 687
Ladeyschikov, D. A., Kirsanova, M. S., Sobolev, A. M., et al. 2021, MNRAS, 506, 4447
Liu, T., Kim, K.-T., Yoo, H., et al. 2016, ApJ, 829, 59
Maíz Apellániz, J., Sota, A., Arias, J. I., et al. 2016, ApJS, 224, 4
Marsh, K. A., Whitworth, A. P., & Lomax, O. 2015, MNRAS, 454, 4282
Marsh, K. A., Whitworth, A. P., Lomax, O., et al. 2017, MNRAS, 471, 2730
Méndez-Delgado, J. E., Amayo, A., Arellano-Córdova, K. Z., et al. 2022, MNRAS, 510, 4436
Moffat, A., Fitzgerald, M., & Jackson, P. 1979, A&AS, 38, 197
Nguyen-Luong, Q., Nakamura, F., Sugitani, K., et al. 2020, ApJ, 891, 66
Nishimura, Y., Shimonishi, T., Watanabe, Y., et al. 2016, ApJ, 829, 94
Ojha, D. K., Samal, M. R., Pandey, A. K., et al. 2011, ApJ, 738, 156
Onus, Adam, Krumholz, Mark R, & Federrath, Christoph 2018, MNRAS, 479, 1702
Pety, J. 2018, Submillimetre Single-dish Data Reduction and Array Combination Techniques (Garching: The European Southern Observatory), 11
Pety, J., Guzmán, V. V., Orkisz, J. H., et al. 2017, A&A, 599, A98
Pineda, J. L., Goldsmith, P. F., Chapman, N., et al. 2010, ApJ, 721, 686
Ripple, F., Heyer, M. H., Gutermuth, R., Snell, R. L., & Brunt, C. M. 2013, MNRAS, 431, 1296
Roman-Duval, J., Heyer, M., Brunt, C. M., et al. 2016, ApJ, 818, 144
Rosolowsky, E., Dunham, M. K., Ginsburg, A., et al. 2010, ApJS, 188, 123
Roueff, A., Gerin, M., Gratier, P., et al. 2021, A&A, 645, A26
Searle, L. 1971, ApJ, 168, 327
Sharpless, S. 1959, ApJS, 4, 257
Shimajiri, Y., André, P., Braine, J., et al. 2017, A&A, 604, A74
Shirley, Y. L. 2015, PASP, 127, 299
Smithsonian Astrophysical Observatory 2000, SAOImage DS9: A utility for displaying astronomical images in the X11 window environment, Astrophysics Source Code Library, record, ascl:0003.002
Sota, A., Maíz Apellániz, J., Morrell, N. I., et al. 2014, ApJS, 211, 10
Stephens, I. W., Jackson, J. M., Whitaker, J. S., et al. 2016, ApJ, 824, 29
van der Walt, Stéfan, Colbert, S Chris, & Varoquaux, Gaël 2011, CSE, 13, 22
Vutisalchavakul, N., Evans, N. J. I., & Heyer, M. 2016, ApJ, 831, 73
Wang, L.-L., Luo, A. L., Hou, W., et al. 2018, PASP, 130, 114301
Wu, J., Evans, N. J. I., Gao, Y., et al. 2005, ApJL, 635, L173
Wu, J., Evans, N. J. I., Shirley, Y. L., & Knez, C. 2010, ApJS, 188, 313
Yadav, R. K., Samal, M. R., Semenko, E., et al. 2022, ApJ, 926, 16
Yasui, C., Kobayashi, N., Saito, M., & Izumi, N. 2016, AJ, 151, 115